Filamentary structures as the origin of blazar jet radio variability

Fuentes, Antonio; Gómez, José L.; Martí, José M.; Perucho, Manel; Zhao, Guang Yao; Lico, Rocco; Lobanov, Andrei P.; Bruni, Gabriele; Gurvits, Leonid I.; More Authors

DOI
10.1038/s41550-023-02105-7

Publication date
2023

Document Version
Final published version

Published in
Nature Astronomy

nature astronomy

Article

https://doi.org/10.1038/s41550-023-02105-7

Filamentary structures as the origin of blazar jet radio variability

Received: 8 February 2023

Accepted: 18 September 2023

Published online: 26 October 2023

Check for updates

Antonio Fuentes[1] ✉, José L. Gómez[1] ✉, José M. Martí[2,3], Manel Perucho[2,3], Guang-Yao Zhao[1], Rocco Lico[1,4], Andrei P. Lobanov[5], Gabriele Bruni[6], Yuri Y. Kovalev[5,7], Andrew Chael[8], Kazunori Akiyama[9,10,11], Katherine L. Bouman[12], He Sun[12], Ilje Cho[1], Efthalia Traianou[1], Teresa Toscano[1], Rohan Dahale[1,13], Marianna Foschi[1], Leonid I. Gurvits[14,15], Svetlana Jorstad[16,17], Jae-Young Kim[5,18,19], Alan P. Marscher[16], Yosuke Mizuno[20,21,22], Eduardo Ros[5] & Tuomas Savolainen[5,23,24]

Supermassive black holes at the centre of active galactic nuclei power some of the most luminous objects in the Universe. Typically, very-long-baseline interferometric observations of blazars have revealed only funnel-like morphologies with little information on the internal structure of the ejected plasma or have lacked the dynamic range to reconstruct the extended jet emission. Here we present microarcsecond-scale angular resolution images of the blazar 3C 279 obtained at 22 GHz with the space very-long-baseline interferometry mission RadioAstron, which allowed us to resolve the jet transversely and reveal several filaments produced by plasma instabilities in a kinetically dominated flow. The polarimetric properties derived from our high-angular-resolution and broad-dynamic-range images are consistent with the presence of a helical magnetic field threaded to the jet. We infer a clockwise rotation as seen in the direction of flow motion with an intrinsic helix pitch angle of ~45° and a Lorentz factor of ~13 at the time of observation. We also propose a model to explain blazar jet radio variability in which emission features travelling down the jet may manifest as a result of differential Doppler boosting within the filaments, as opposed to the standard shock-in-jet model. Characterizing such variability is particularly important given the relevance of blazar physics from cosmic particle acceleration to standard candles in cosmology.

We observed 3C 279 on 10 March 2014 at 22 GHz (1.3 cm) with the space very-long-baseline interferometry (VLBI) mission RadioAstron[1], a 10 m space radio telescope onboard the Spektr-R satellite and an array of 23 ground-based radio telescopes spanning baseline distances from hundreds of kilometres to the Earth's diameter (see Methods for a description of the array). The highly eccentric orbit of the space radio telescope, with an apogee of ~350,000 km, provided us with ground-space fringe detections of the source up to a projected baseline distance of eight Earth diameters, probing a wide range of spatial frequencies perpendicular to the jet propagation direction (Extended Data Fig. 1). At the longest projected baselines to RadioAstron, we achieved a resolving power of 27 μas, similar to that obtained by the Event Horizon Telescope (EHT) at 1.3 mm (~20 μas)[2]. The large number of detections reported within the RadioAstron active galactic nuclei (AGN) survey

A full list of affiliations appears at the end of the paper. ✉e-mail: afuentes@iaa.es; jlgomez@iaa.es

https://doi.org/10.1038/s41550-023-02105-7

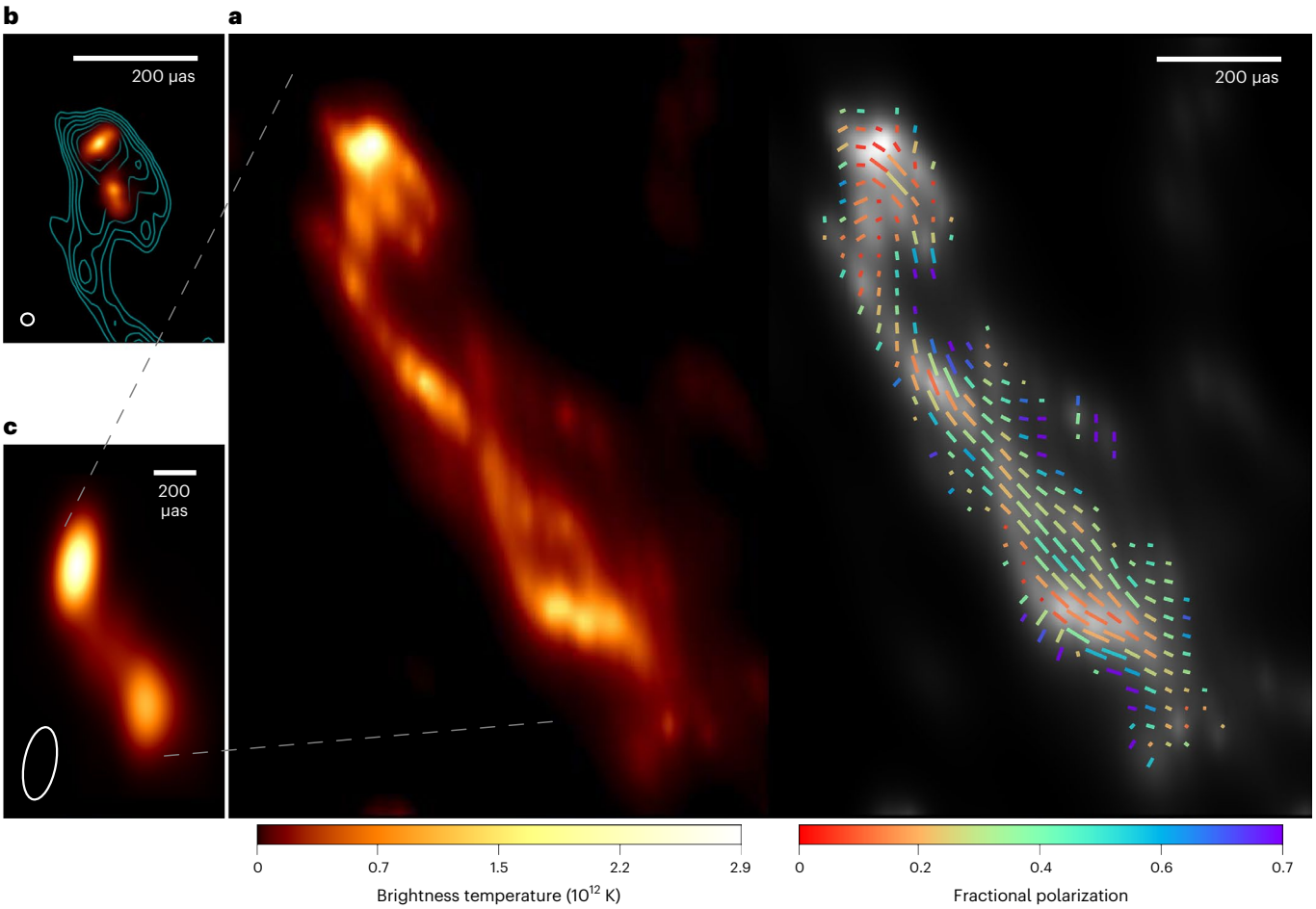

Fig. 1 | The filamentary structure of the jet in 3C 279 revealed by RadioAstron. **a**, Total intensity (left) and linearly polarized (right) RadioAstron image at 1.3 cm obtained on 10 March 2014. While both images in **a** show brightness temperature (colour scale), the image on the right also shows the recovered electric vector position angles overlaid as ticks. Their length and colour are proportional to the level of linearly polarized intensity and fractional polarization, respectively. **b**, The 1:1 scale 1.3 mm EHT image obtained in April 2017. Contours correspond to our RadioAstron image, and are shown to compare the different scales probed. These start at 90% of the peak brightness and decrease by successive factors of 3/2 until they reach 5%. Both images were aligned with respect to the pixel with maximum brightness. **c**, The 7 mm VLBA-BU-BLAZAR programme image obtained on 25 February 2014. White ellipses at the bottom-left corners of **b** and **c** indicate the 20 × 20 μas^2 and 150 × 360 μas^2 convolving beams, respectively. The colour bars refer only to information displayed in **a**.

programme[3] made 3C 279 an ideal target for detailed imaging. Figure 1 presents our RadioAstron space VLBI polarimetric image of the blazar 3C 279. A representative image reconstruction obtained using new regularized maximum likelihood methods[4,5] is shown along with the closest-in-time 7 mm VLBA-BU-BLAZAR programme image obtained on 25 February 2014, and the 1.3 mm EHT image obtained in April 2017. We show a field of view of around 1 × 1 mas^2 with an image total flux density of 27.16 Jy, and note that all extended emission outside this region is resolved out by RadioAstron. The robustness of our image is demonstrated in Extended Data Fig. 2, where we show how it fits the data used for both total intensity and linearly polarized image reconstruction. We acknowledge, however, that VLBI imaging is an ill-posed problem, and any image reconstruction that fits the data is not unique (for example, see the comprehensive image analysis carried out in ref. 6). The image in Fig. 1 is complemented by the 48 images presented in Extended Data Fig. 3. In Extended Data Fig. 4 we also demonstrate our ability to reconstruct thin filamentary structures with RadioAstron using synthetic data (see the Methods for a detailed description).

In contrast to the contemporaneous 7 mm and classical millimetre- and centimetre-wave VLBI jet images[7,8], in which the observed synchrotron emission seems to be contained in a funnel with a uniform cross-section, we show in great detail the internal structure of a blazar jet and find strong evidence for the filamentary nature of the emitting regions within it. We identify the jet core as the upstream bright component, and the so-called core region encompasses approximately the inner 200 μas, roughly the extent of the features probed at 1.3 mm. The base is slightly elongated and tilted in the southeast–northwest direction, as reported in ref. 2. However, contrary to the EHT sparse sampling of the Fourier plane[2,9], the ground array supporting our space VLBI observations provided a substantially larger filling fraction, which enabled us to reconstruct images with a dynamic range that is two orders of magnitude larger. Thus, while we can recover up to three different filaments emanating perpendicularly from the jet base, the EHT could only recover one and is 'blind' to the extended, filamentary structure, primarily due to the lack of short baselines. In fact, the peak flux density ratio between the core and extended jet measured at 7 mm changes from ~1.5 in February 2014 to ≥10 in April 2017. If aligned with respect to the brightness peak, both images match remarkably well, and the jet feature observed at 1.3 mm is coincident in position and extension with our central filament, ignoring the small ($\lesssim$35 μas) core shift between the two frequencies[10]. Within our uncertainty, we do not measure a substantial change in the core position angle with respect to the EHT image, taken 3 years later. The single-epoch results presented here do not allow us to discern whether this elongated structure corresponds

https://doi.org/10.1038/s41550-023-02105-7

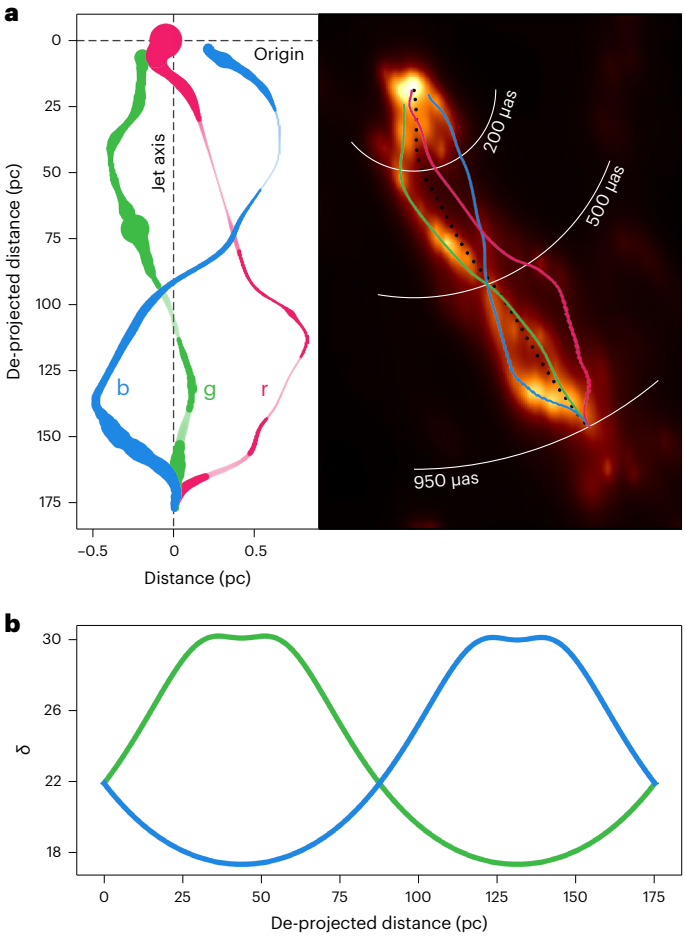

Fig. 2 | Analysis of the recovered filamentary structure. a, Left: de-projected filament coordinates fitted using three Gaussian curves (darker shading; Methods). Lighter shading indicates regions where the coordinates have been interpolated. The marker size scales with the flux density. Note that the *x*- and *y*-axis scales are different. Right: position of the fitted filaments overlaid on the reconstructed image. Colour scale as in Fig. 1. The black dotted curve denotes the main jet axis. **b**, Doppler factor computed for plasma propagating along a double thread, as is expected for elliptical modes, with $\Gamma = 13$ and $\theta = 1.9°$.

to the accretion disk or to another extended jet component. Nonetheless, based on the small viewing angle inferred[11] ($\theta \approx 1.9°$) and the multi-epoch kinematic analysis of the model-fitted jet components, ref. 2 raised the possibility of this structure corresponding to a sharply bent part of the inner jet.

Moving beyond the core region, in Fig. 2a we show the de-projected and on-sky coordinates of the two main filaments (hereafter g and b), and a possible third filament (r), obtained from the fitting of three Gaussian curves to transverse cuts to the main jet axis (Methods). Further downstream, filament g is continuously recovered and contains most of the eastern extended structure flux density. Initially propagating in the southern direction, it displays a sharp bend of ~45° to the west, close to the core region boundary. Although not continuously, we are also able to reconstruct filament b beyond the inner 200 μas in what seems to be a helical-like morphology. These two filaments converge at ~500 μas down the jet, where filament b crosses over g. Further downstream, they bend and converge again at ~950 μas, where the brightness of the weaker filament is largely enhanced as it bends, now dominating the reconstructed emission in the southernmost jet region. Some diffuse emission is also systematically recovered parallel to filament g after the first crossing, which might indicate the presence of a third filament (r).

As detailed in the Methods, there is a physically consistent domain in the space of parameters (Γ, a_j/a_{ex}; where a_j is the sound speed of the jet flow and a_{ex} is the sound speed of the ambient medium), where the Lorentz factor Γ is within the previously determined range of jet flow Lorentz factor for 3C 279 (ref. 12) ($\Gamma \in [10, 40]$), which allowed us to interpret the observed approximate spatial periodicity, λ_m, as the wavelength of the elliptical surface mode of a kinetically dominated, cold jet. More intriguing is the fact that the filaments associated with the elliptical mode are brighter in particular locations separated by half a wavelength (~400 μas for filament g, ~850 μas for filament b), just before the crossings of the filaments. The properties of the flow (for example, pressure, density, flow velocity) are modified locally by the elliptical wave, with the magnitude of the changes depending on the position and time as modulated by the wave phase. Such small changes in the properties of the flow could explain the differences in brightness between regions inside the jet and, in particular, along the filaments. Here the perturbation in the three-velocity vector and the subsequent changes in the local Doppler boosting play a major role. Figure 2b shows how the Doppler factor, δ, evolves along two threads originated by an elliptical mode in a plasma characterized by $\Gamma = 13$ and $\theta = 1.9°$. With a ratio $\delta_{max}/\delta_{min} \simeq 1.7$, the brightness of certain regions can increase by a factor of ~5, in agreement with the brightness excess observed at ~400 μas in filament g, and at ~850 μas in filament b. This enhanced emission would then be the result of the Doppler boosted emission along the line of sight. This interpretation is supported by the fact that both enhanced emission regions are found at approximately the same phase of the corresponding helical filament, with the local flow velocity pointing along the same direction (the line of sight).

Continuing with this interpretation, it is important to note that the enhanced emission regions will not be steady but will propagate downstream at a (pattern) speed equal to the wave's phase velocity. The fact that these brighter regions in filaments g and b match the jet features observed at 7 mm (components C32 and C31 in refs. 11,13, respectively) suggests the appealing possibility that these features correspond to the propagation of an elliptical perturbation mode, and not to the propagation of a shock, as proposed by the standard shock-in-jet model[14]. In particular, the estimated apparent speed of ~7.23 *c* (component C31, ref. 11), corresponding to a propagation speed of ~0.996 *c* ($\Gamma \simeq 11$) and close to the lower limit of the 3C 279 jet Lorentz factor estimates, supports this possibility as these waves propagate downstream along the jet with velocities smaller than or equal to that of the jet bulk flow (see refs. 15,16 and the Methods). We illustrate our proposed model for the jet variability in 3C 279 in the schematic in Fig. 3. Likewise, filamentary structures triggered by plasma instabilities could explain the variability observed at radio wavelengths in other blazar sources and, in some cases, they could coexist with components originating from shock waves. An important implication of our study is that the main emission occurs in thin filaments that cover only a fraction of the jet cross-section. The timescale of variability of such features can therefore be much shorter than the light-travel time across the entire jet width, a fact that can help to explain the extremely rapid variability reported in gamma-rays[17]. We note that while our findings and proposed model come from the first spatially resolved image of a blazar internal structure, similar models based on differential Doppler boosting effects have also been suggested from indirect measurements (for example, see ref. 18). In the case of 3C 279, magnetic reconnection has recently been proposed[19] as the mechanism behind gamma-ray flares, as opposed to shock waves or geometric effects. Nonetheless, the variability we model, as it originates from the formation of filamentary structures triggered in a kinetically dominated jet flow, concerns only that observed at radio wavelengths beyond the inner core region.

The analysis of the linearly polarized emission captured by RadioAstron and the supporting ground array reveals clear signatures of a toroidal magnetic field threaded to the relativistic jet. The source is mildly polarized, with an integrated degree of linear polarization of ~10%.

https://doi.org/10.1038/s41550-023-02105-7

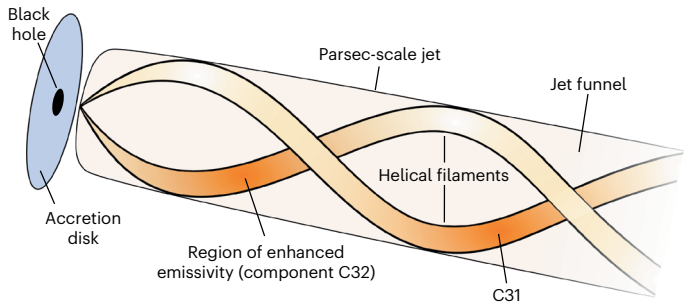

Fig. 3 | The proposed model for the internal jet structure in 3C 279. The development of plasma instabilities within the jet flow leads to filamentary structures with heterogeneous emissivity. Local changes in the plasma properties, which evolve and travel down the jet with the wave velocity, can explain these commonly observed moving components as a result of differential Doppler boosting.

The electric vector position angle indicates a magnetic field predominantly perpendicular to the flow propagation direction—that is, consistent with a helical magnetic field dominated by its toroidal component. However, the presence of a helical magnetic field usually implies that Faraday rotation measure gradients are found across the jet width[20–22]. Future joint analysis of RadioAstron 22 GHz and VLBA 43 GHz polarimetric images will further test this. Relativistic magnetohydrodynamic simulations of jets at parsec scales have shown that, in the presence of a helical magnetic field, the observed synchrotron emission is unevenly distributed across the jet width[23–26]. Based on the strong asymmetry in the reconstructed emission between the eastern and western sides of the jet axis, and following the analysis described in the Methods, we can infer a jet bulk flow Lorentz factor of $\Gamma \simeq 13$, which is in excellent agreement with the estimates provided by analysing the kinematics of the parsec-scale jet. Moreover, this allows us to further infer a possible helical magnetic field, with an intrinsic pitch angle of ~45°, rotating clockwise as seen in the direction of flow motion.

The findings presented in this Article, supported by previous VSOP (for example, refs. 27,28) and RadioAstron (for example, refs. 29,30) space VLBI observations, strongly suggest that blazar jets have a complex and rich internal structure beyond the funnel-like morphologies reported by ground-based VLBI studies at lower angular resolutions. Future space VLBI missions and enhanced millimetre-wave global arrays, which will enable high-dynamic-range observations capable of spatially resolving the jet width, should prove decisive in determining the true nature of jets powered by supermassive black holes.

Methods

Observations

Observations of 3C 279 were conducted at 22.2 GHz (1.3 cm) on 2014 March 10–11, spanning a total of 11 h 44 min from 14:15 to 01:59 UT. During the observing session, RadioAstron recorded evenly spaced (every 80–90 min) blocks of data of 30 min and one final block of ~2 h, corresponding to its orbit perigee. This allowed the spacecraft to cool down its high-gain antenna drive between observing segments. Together with RadioAstron, a ground array of 23 antennas observed the target: ATCA, Ceduna, Hobart, the Korean VLBI Network antennas Tanman, Ulsan and Yonsei, Mopra, Parkes, Sheshan, Badary, Urumqi, Hartebeesthoek, Kalyazin, Metsähovi, Noto, Torun, Medicina, Onsala, Yebes, Jodrell Bank, Effelsberg, Svetloe and Zelenchukskaya.

Left- and right-circularly polarized (LCP and RCP, respectively) signals were recorded simultaneously at each station, with a total bandwidth of 32 MHz per polarization. The collected data were then processed at the Max-Planck-Institut für Radiostronomie using the upgraded version of the DiFX correlator[31]. Fringes between RadioAstron and ground stations were searched using the largest dishes, separately for each scan. This provided a first-order clock correction that was later refined with baseline stacking in AIPS[32]. When no signal was found, we adopted a best-guess clock value extrapolated from scans giving fringes, with the aim of performing a further global fringe search at a later stage with AIPS.

Data reduction

For the initial data reduction, we used ParselTongue[33], a Python interface for AIPS. In the first stage, we performed an a priori calibration of the correlated visibility amplitudes using the system temperatures and gain curves registered at each station. Some of the antennas participating in the observations failed to deliver system temperature information, which we compensated by using nominal values modulated by the antenna's elevation at each scan. As we chose the average system temperature as the station's default value, visibility amplitudes were not properly scaled. We overcame this issue by determining, every 2 min, the gain corrections needed for each intermediate frequency and polarization from a preliminary image in which only closure quantities (closure phases and log-closure amplitudes) were involved, using the SMILI software library[34,35]. We then applied to each antenna the mean gain value obtained, allowing further residual corrections to be made during the final imaging and self-calibration. The image total flux density was fixed to that measured by the intra-Korean VLBI Network baselines (27.65 Jy), whose a priori calibration was excellent[36]. Finally, we corrected the phase rotation introduced by the receiving systems as the source's parallactic angle changes.

We then solved for residual single- and multi-band delays, phases and phase rates by incrementally fringe-fitting the data. In the first iteration we excluded RadioAstron and performed a global fringe search on the ground array with a solution interval of 60 s using Mopra and Effelsberg as reference antennas for the first and second part of the experiment, respectively. Once fully calibrated, the ground array was coherently combined (trough baseline stacking) to increase the signal-to-noise ratio of possible fringe detections to RadioAstron. To account for the acceleration of the spacecraft near its perigee and the low sensitivity of the longest projected baseline lengths to it, we adopted different solution intervals (from 10 s to 240 s) and data total bandwidth (by combining intermediate frequencies). With a signal-to-noise ratio cutoff of 5, reliable ground-space fringes were detected at distances of up to ~8 Earth diameters, corresponding to the first observing block of RadioAstron (from 14:15 to 14:45 UT), providing a maximum angular resolution of 27 μas in the direction transverse to the jet axis. Finally, we solved for the antennas' bandpasses, the delay differences between polarizations using the task RLDLY, and exported the frequency-averaged data along each intermediate frequency. The fringe-fitted visibility coverage in the Fourier plane is shown in Extended Data Fig. 1.

Imaging

Imaging of the data was carried out using novel regularized maximum likelihood (RML) methods[37], implemented in the eht-imaging software library[4,5]. While the CLEAN algorithm[38] has been widely used in the past for VLBI image reconstruction, RML methods are not extensively used, especially at centimetre wavelengths and for space VLBI experiments. Generally speaking, RML methods try to solve for the image I, constrained by the measurements V, that minimizes an objective function J defined as follows:

$$J(I) = \sum_{\text{data terms}} \alpha_D \chi^2_D(I, V) - \sum_{\text{reg. terms}} \beta_R S_R(I), \quad (1)$$

where D and R are a set of selected data products and regularization terms, respectively, and α_D and β_R are hyperparameters that weight the contribution of the image fitting to the data χ^2_D, and the image-domain regularization S_R, to the minimization of the previous equation.

Contrary to traditional CLEAN algorithm, full closure data products (closure phases and log closure amplitudes) can be employed during image reconstruction in addition to complex visibilities, further constraining the proposed image. Given the large number of telescopes participating in the experiment, closure quantities have proved quite useful as atmospheric phase corruption and gain uncertainties are mitigated. Multiple regularization over the proposed image can be imposed too, such as smoothness between adjacent pixels or similarity to a prior image.

Before imaging, we performed an initial phase-only self-calibration to a point source model with a solution interval of 5 s and coherently averaged the data in 120 s intervals using the DIFMAP package[39]. We compared these results with those obtained with the AIPS task CALIB, for which a signal-to-noise ratio cutoff of 5 was set, to ensure that no artificial signal was introduced into the data. In the following paragraphs we describe the imaging procedure.

As a first a step, we flagged all baselines to RadioAstron and imaged the data collected only by ground radio telescopes. The pre-processed data noise budget was inflated by a small amount (1.5%), to account for non-closing errors, and the image was initialized with an elliptical Gaussian oriented at roughly the same angle as the 7 mm image and enclosed in a 1.5×1.5 mas^2 field of view gridded by 200×200 pixels. As mentioned above, because of the poor a priori amplitude calibration due to missing antennas' system temperatures, we opted for a first round of imaging in which only closure quantities (closure phases and log closure amplitudes) were used to constrain the image likelihood. This likelihood took the form of the mean squared standardized residual (similar to a reduced χ^2) as defined in ref. 6. Each imaging iteration took the image reconstructed in the previous step as its initial guess blurred to the nominal resolution of the ground array (that is, 223 μas), which prevented the algorithm getting caught in local minima during the optimization of equation (1). We then self-calibrated the data to the closure-only image obtained and incorporated full complex visibilities in the imaging process, which was finalized by repeating the imaging and self-calibration cycle two more times. In addition to the data products mentioned, we imposed several regularizations on the proposed images. These included maximum entropy (mem), which favoured similarity to a previous image; total variation (tv) and total squared variation (tv2), which favoured smoothness between adjacent pixels; ℓ_1 − norm, which favoured sparsity in the image; and total flux regularization, which encouraged a certain total flux density in the image. Finally, we restored all baselines to RadioAstron and repeated this procedure, substituting the Gaussian initialization with the blurred, ground-only image previously reconstructed and using the full array nominal resolution (27 μas) between imaging iterations to blur intermediate reconstructions.

In contrast to full Bayesian methods, RML techniques do not estimate the posterior distribution of the underlying image, but instead compute the maximum a posteriori solution; that is, the single image that best minimized equation (1). The hyperparameters chosen will inevitably have an impact on the reconstructed image features, thus we conducted a scripted parameter survey to ensure the robustness of the subtle structures seen in Fig. 1 and to impartially determine which parameters performed better in the image reconstruction. From the many images obtained, we show in Extended Data Fig. 3 the complete collection of images that could potentially describe the observed source structure. These fitted the data equally well and preserved the total flux measured by the Korean VLBI Network to a certain level. The regularizers and hyperparameters used to obtain these images are listed in each panel of Extended Data Fig. 3. Apart from these, we gave the same weight to complex visibilities and closure quantity data terms. Although we observed some differences in the weaker emission, the main filamentary structure was present in all the images. Figure 1 corresponds to no. 21, which had the overall minimum reduced χ^2.

Synthetic data tests

Given that one of the helical filaments reconstructed in our images (filament b) crosses over the other with a position angle roughly oriented in the direction where we lack space–ground baseline coverage, we tested the ability of the image reconstruction algorithm to successfully recover similarly oriented structures. With that aim, we generated two synthetic datasets using eht-imaging (for example, see refs. 6,40). These simulated space VLBI observations of the source models presented in Extended Data Fig. 4 with the same baseline coverage as that in Extended Data Fig. 1. The datasets were corrupted with thermal noise and the visibility phases were scrambled. These simple geometric models were specially designed to mimic the crossing of two helical filaments and to some extent the brightness distribution of the 3C 279 images reconstructed. While the first model was oriented as the parsec-scale jet in 3C 279, the second model was oriented perpendicularly to the fitted beam position angle (-10°).

In Extended Data Fig. 4 we show the images reconstructed following the procedure described in the previous section. For comparison, we also present the images obtained after flagging all RadioAstron baselines; that is, with only the ground array. When the full array was considered, we were able to fully recover the crossing of the filaments and ground-truth structure of the model oriented in the same way as the jet in 3C 279, although we acknowledge the poorer performance in reconstructing the internal structure of the model oriented perpendicularly to the position angle of the fitted beam, as expected. On the contrary, when space–ground baselines are removed, the images reconstructed display a jet correctly oriented but with no traces of helical filaments. Thus, we are confident that the recovered filamentary structure, only achievable at this observing frequency thanks to RadioAstron, is derived from the intrinsic source structure and not from the lack of north–south space–ground baselines.

Polarimetric imaging

The polarization results presented in Fig. 1 were also obtained using the eht-imaging library. A more complete description of the method can be found in refs. 4,41, here we briefly outline the procedure followed. For polarimetric imaging, eht-imaging minimizes equation (1), substituting complex visibilities and closure quantities data terms by polarimetric visibilities $\mathcal{P} = \tilde{Q} + i\tilde{U}$ and the visibility domain polarimetric ratio $\breve{m} = \mathcal{P}/\tilde{\mathcal{I}}$, constructed using the visibility-domain Stokes parameters $\tilde{I}$, $\tilde{Q}$, and $\tilde{U}$. Note that total intensity and linearly polarized intensity images were reconstructed independently. Image regularization then included total variation, which, as for total intensity imaging, encouraged smoothness between adjacent pixels, and the Holdaway–Wardle regularizer[42], which prefers pixels with polarization fraction values below the theoretical maximum of 0.75. The pipeline then alternated between minimizing the polarimetric objective function and solving for the complex instrumental polarization, the so-called D terms. The instrumental polarization calibration was performed by maximizing the consistency between the self-calibrated data and sampled data from corrupted image reconstructions. After D-term solutions were found for each antenna, the reconstructed polarimetric image was blurred, as was done for Stokes $\mathcal{I}$ imaging, and the imaging-calibration cycle was repeated until the solutions converged.

In addition to instrumental polarization, VLBI polarimetric analyses rely on the calibration of the absolute polarization angle. To account for this, we compared our polarization results with the closest-in-time 7 mm results. The recovered polarization angle patterns matched remarkably well when our image was convolved with the 7 mm beam. Ignoring Faraday rotation of the polarization angle between the two frequencies, based on the small rotation measure values reported in refs. 43,44, we estimated an overall median difference of ~8° that we applied to the results presented in Fig. 1.

Filament fitting

The relative right ascension and declination of the filaments were obtained by fitting three Gaussian curves to transverse profiles of the brightness distribution. We first computed the main jet axis, commonly referred to as the ridge line, from a convolved version of the reconstructed image. Using a sufficiently large Gaussian kernel, we blurred our image until the emission blended into a unique stream and the filaments were no longer distinguishable, similarly to the 7 mm VLBA-BU-BLAZAR image. We then projected this image into polar coordinates, centred at the jet origin, and sliced it horizontally, storing the position of the flux density peak for each cut. These positions were then transformed back to Cartesian coordinates, providing the main jet axis. To each pair of consecutive points conforming the axis, we computed the local perpendicular line and retrieved the flux density of the pixels contained in the cut. With this procedure, we assembled a set of transverse brightness profiles to which we fitted the sum of three Gaussian curves using the python package lmfit[45]. The number of Gaussian components used was motivated by the number of filaments observed emanating from the core region, although we note that two Gaussian components were enough to fit the two main threads. Finally, we selected the coordinates as the position of the peak(s) found in the curve best fitting each cut. In Fig. 2, coordinates were de-projected assuming a source redshift $z = 0.536$ (ref. 46), a viewing angle $\theta = 1.9°$ (ref. 11) and a cosmology $H_0 = 67.7\ \mathrm{km\ s^{-1}\ Mpc^{-1}}$, $\Omega_m = 0.307$ and $\Omega_\Lambda = 0.693$ (ref. 47), where H_0 is the Hubble constant, and Ω_m and Ω_Λ are the matter and dark energy density parameters, respectively.

Instability analysis

Based on the aforementioned Gaussian fitting to the observed filaments, we estimated an approximate spatial periodicity λ_m of 950 μas (projected on the plane of the sky) or 175 pc (de-projected), which corresponded to ~2.3×10^6 gravitational radii assuming a black hole mass of $M_\mathrm{BH} \simeq 8 \times 10^8\ M_\odot$ (ref. 48). The possibility of these filaments reflecting a fundamental periodicity of the black hole or inner accretion disk directly associated with their rotation should be dismissed, as it would imply propagation speeds along the filaments larger than the speed of light by orders of magnitude. At the same time, explanations of such a fundamental periodicity in terms of the precession of a jet nozzle, caused by the Lense–Thirring effect[49] or a supermassive black hole binary system, invoked to explain a sharp bend in the nuclear region, have recently been refuted[2]. On the other hand, anchoring the filaments to the outer accretion disk to allow a subluminal propagation of the helical pattern would imply an exceedingly large (Keplerian) disk radius—that is, larger than ~1 light yr, which is about two orders of magnitude larger than the expected disk sizes[50].

According to ref. 2, the jet no longer accelerates beyond ~100 μas from the core, suggesting a kinetically dominated flow in which the observed filaments show a magnetic field structure dominated by the toroidal component. Taking this into account, we conclude that these bright filaments reveal compressed regions with enhanced gas and magnetic pressure—favouring an increased synchrotron emissivity and ordering of the magnetic field. Thus, these might be associated with the triggering and development of flow instabilities. Current-driven kink or Kelvin–Helmholtz instabilities are the most plausible mechanisms for developing such helical structures[16,28,51]. Rayleigh–Taylor instabilities have also been discussed in the context of jet expansion and recollimation as a possible trigger of small-scale distortions of the jet surface and turbulent mixing (see ref. 52 for a review). However, Rayleigh–Taylor instabilities would not produce filaments like the ones we observe, so we neglect this option. Current-driven instabilities dominate in Poynting-flux regimes with strong helical magnetic fields; that is, in the jet's acceleration and collimation region. Kelvin–Helmholtz instabilities, however, have the largest growth in kinetically dominated flows, and are thus favoured in our case. The extension of the filaments greatly exceeds the jet radius, which is expected for Kelvin–Helmholtz surface modes. While two filaments could be generated by an elliptical mode, the possible third filament observed might indicate the presence of an additional helical mode interfering with the elliptical.

Assuming that the jet is kinetically dominated and cold, as expected for powerful jets that are already expanded and accelerated, the fastest growing frequency of a mode is given by $\omega^*_{nm} R/a_\mathrm{ex} = (n + 2m + 1/2)\pi/2$ (refs. 15,53; quantities with a superscript asterisk refer to resonant, or fastest growing, modes), where R is the radius and n and m are the types of mode ($n = 1, 2$ for helical and elliptical modes, respectively; and $m = 0$ for a surface mode). Taking $\omega \leq 2\pi c/\lambda_\mathrm{m}$, we found $a_\mathrm{ex} \approx 10^{-2}\ c$ for both the helical and elliptical modes. At this maximum growth frequency, and for a highly supersonic jet (that is, with a jet Mach number $M_\mathrm{j} \gg 1$), the wavelength of the mode and wave velocity are given, respectively, by:

$$\lambda^*_\mathrm{m} \approx \frac{4}{n+1/2} M_\mathrm{ex} \frac{\Gamma}{a_\mathrm{j}/a_\mathrm{ex} + \Gamma} R \tag{2}$$

$$v^*_\mathrm{w} \approx \frac{\Gamma}{a_\mathrm{j}/a_\mathrm{ex} + \Gamma} u, \tag{3}$$

where u is the jet flow velocity (which approximates the light speed c given the large Lorentz factors inferred), Γ is the jet flow Lorentz factor and M_ex is the Mach number of the jet with respect to the ambient sound speed ($M_\mathrm{ex} = u/a_\mathrm{ex} \approx c/a_\mathrm{ex} \approx 100$).

In our interpretation, described in the main text, the wave velocity v^*_w coincides with the (pattern) speed of the jet feature observed at 7 mm (component C31 in ref. 11), very close to c, leading to the condition (see equation (3)) $a_\mathrm{j}/a_\mathrm{ex} \ll \Gamma$ or, equivalently, $M_\mathrm{j} \gg M_\mathrm{ex}/\Gamma$. With $M_\mathrm{ex} \approx 100$ and $\Gamma \in [10, 40]$, the last condition implies $M_\mathrm{j} \gg 1$, hence validating our assumption of a kinetically dominated flow at the observed scales.

Jet properties derived from the reconstructed polarimetric emission

The synchrotron radiation coefficients are a function of the angle between the magnetic field and the line of sight in the fluid frame. Thus, for a fixed viewing angle and jet flow velocity, the bulk of the emission will be located on either side of the main jet axis, depending on the magnetic field helical pitch angle. This asymmetry is maximized when the helical magnetic field pitch angle (in the fluid frame) ϕ' is 45° (ref. 23). Given the strong asymmetry in the reconstructed emission between the eastern and western sides of the jet axis, we could assume that the viewing angle in the fluid's frame approximates ϕ' (that is, $\theta' \simeq \phi'$). Hence, given the estimated viewing angle in the observer's frame ($\theta \approx 1.9°$) (ref. 11) and the light aberration transformations[54]

$$\sin\theta' = \frac{\sin\theta}{\Gamma(1-\beta\cos\theta)}, \quad \cos\theta' = \frac{\cos\theta - \beta}{1-\beta\cos\theta}, \tag{4}$$

where $\beta = \sqrt{1 - 1/\Gamma^2}$, we can infer a jet bulk flow Lorentz factor of $\Gamma \simeq 13$, which is in excellent agreement with the estimates provided by analysing the kinematics of the parsec-scale jet[11], and satisfies the upper limit previously established by our Kelvin–Helmholtz instability analysis. Moreover, this allowed us to estimate the viewing angle θ_r at which the emission asymmetry will reverse from one side to the other as $\cos\theta_\mathrm{r} = (1 - 1/\Gamma^2)^{1/2}$ (ref. 23), which results in $\theta_\mathrm{r} \simeq 4.4°$ for $\Gamma = 13$. Given that $\theta < \theta_\mathrm{r}$ and the bulk of the reconstructed emission is located to the east of the jet axis, we infer a helical magnetic field rotating clockwise as seen in the direction of flow motion. The Lorentz transformation of the magnetic field from the fluid's to the observer's frame boosts the toroidal component by Γ (ref. 55), and therefore the helix pitch angle transforms as $\tan\phi = \Gamma \tan\phi'$. This means that $\phi \simeq 86°$ in the observer frame, which is in agreement with the predominantly toroidal magnetic field observed.

Data availability

The pre-processed dataset used for imaging is available via Github at https://github.com/aefez/radioastron-3c279-2014.

Code availability

The software packages used to calibrate, image and analyse the data are available at the following websites: AIPS, http://www.aips.nrao.edu/index.shtml; ParselTongue (https://www.jive.eu/jivewiki/doku.php?id=parseltongue:parseltongue), DIFMAP (https://science.nrao.edu/facilities/vlba/docs/manuals/oss2013a/post-processing-software/difmap), SMILI (https://github.com/astrosmili/smili), eht-imaging (https://github.com/achael/eht-imaging) and lmfit (https://lmfit.github.io/lmfit-py/).

References

1. Kardashev, N. S. et al. 'RadioAstron'—a telescope with a size of 300 000 km: main parameters and first observational results. *Astron. Rep.* **57**, 153–194 (2013).
2. Kim, J.-Y. et al. Event Horizon Telescope imaging of the archetypal blazar 3C 279 at an extreme 20 microarcsecond resolution. *Astron. Astrophys.* **640**, A69 (2020).
3. Kovalev, Y. et al. Detection statistics of the RadioAstron AGN survey. *Adv. Space Res.* **65**, 705–711 (2020).
4. Chael, A. A. et al. High-resolution linear polarimetric imaging for the Event Horizon Telescope. *Astrophys. J.* **829**, 11 (2016).
5. Chael, A. A. et al. Interferometric imaging directly with closure phases and closure amplitudes. *Astrophys. J.* **857**, 23 (2018).
6. Event Horizon Telescope Collaboration et al. First M87 Event Horizon Telescope results. IV. Imaging the central supermassive black hole. *Astrophys. J. Lett.* **875**, L4 (2019).
7. Jorstad, S. G. et al. Polarimetric observations of 15 active galactic nuclei at high frequencies: jet kinematics from bimonthly monitoring with the Very Long Baseline Array. *Astron. J.* **130**, 1418–1465 (2005).
8. Lister, M. L. et al. MOJAVE: monitoring of jets in active galactic nuclei with VLBA experiments. V. Multi-epoch VLBA images. *Astron. J.* **137**, 3718–3729 (2009).
9. Event Horizon Telescope Collaboration et al. First M87 Event Horizon Telescope results. II. Array and instrumentation. *Astrophys. J. Lett.* **875**, L2 (2019).
10. Pushkarev, A. B. et al. MOJAVE: monitoring of jets in active galactic nuclei with VLBA experiments. IX. Nuclear opacity. *Astron. Astrophys.* **545**, A113 (2012).
11. Jorstad, S. G. et al. Kinematics of parsec-scale jets of gamma-ray blazars at 43 GHz within the VLBA-BU-BLAZAR program. *Astrophys. J.* **846**, 98 (2017).
12. Bloom, S. D., Fromm, C. M. & Ros, E. The accelerating jet of 3C 279. *Astron. J.* **145**, 12 (2013).
13. Weaver, Z. R. et al. Kinematics of parsec-scale jets of gamma-ray blazars at 43 GHz during 10 yr of the VLBA-BU-BLAZAR program. *Astrophys. J. Suppl. Ser.* **260**, 12 (2022).
14. Marscher, A. P. & Gear, W. K. Models for high-frequency radio outbursts in extragalactic sources, with application to the early 1983 millimeter-to-infrared flare of 3C 273. *Astrophys. J.* **298**, 114–127 (1985).
15. Hardee, P. E. On three-dimensional structures in relativistic hydrodynamic jets. *Astrophys. J.* **533**, 176–193 (2000).
16. Vega-García, L., Perucho, M. & Lobanov, A. P. Derivation of the physical parameters of the jet in S5 0836+710 from stability analysis. *Astron. Astrophys.* **627**, A79 (2019).
17. Hayashida, M. et al. Rapid variability of blazar 3C 279 during flaring states in 2013-2014 with joint Fermi-LAT, NuSTAR, Swift, and ground-based multiwavelength observations. *Astrophys. J.* **807**, 79 (2015).
18. Raiteri, C. M. et al. Blazar spectral variability as explained by a twisted inhomogeneous jet. *Nature* **552**, 374–377 (2017).
19. Shukla, A. & Mannheim, K. Gamma-ray flares from relativistic magnetic reconnection in the jet of the quasar 3C 279. *Nat. Commun.* **11**, 4176 (2020).
20. Gabuzda, D. C., Murray, É. & Cronin, P. Helical magnetic fields associated with the relativistic jets of four BL Lac objects. *Mon. Not. R. Astron. Soc.* **351**, L89–L93 (2004).
21. Broderick, A. E. & McKinney, J. C. Parsec-scale Faraday rotation measures from general relativistic magnetohydrodynamic simulations of active galactic nucleus jets. *Astrophys. J.* **725**, 750–773 (2010).
22. Pasetto, A. et al. Reading M87's dna: a double helix revealing a large-scale helical magnetic field. *Astrophys. J. Lett.* **923**, L5 (2021).
23. Aloy, M.-A., Gómez, J.-L., Ibáñez, J.-M., Martí, J.-M. & Müller, E. Radio emission from three-dimensional relativistic hydrodynamic jets: observational evidence of jet stratification. *Astrophys. J. Lett.* **528**, L85–L88 (2000).
24. Fuentes, A., Gómez, J. L., Martí, J. M. & Perucho, M. Total and linearly polarized synchrotron emission from overpressured magnetized relativistic jets. *Astrophys. J.* **860**, 121 (2018).
25. Moya-Torregrosa, I., Fuentes, A., Martí, J. M., Gómez, J. L. & Perucho, M. Magnetized relativistic jets and helical magnetic fields. I. Dynamics. *Astron. Astrophys.* **650**, A60 (2021).
26. Fuentes, A., Torregrosa, I., Martí, J. M., Gómez, J. L. & Perucho, M. Magnetized relativistic jets and helical magnetic fields. II. Radiation. *Astron. Astrophys.* **650**, A61 (2021).
27. Lobanov, A. P. & Zensus, J. A. A cosmic double helix in the archetypical quasar 3C273. *Science* **294**, 128–131 (2001).
28. Perucho, M., Kovalev, Y. Y., Lobanov, A. P., Hardee, P. E. & Agudo, I. Anatomy of helical extragalactic jets: the case of S5 0836+710. *Astrophys. J.* **749**, 55 (2012).
29. Bruni, G. et al. RadioAstron reveals a spine-sheath jet structure in 3C 273. *Astron. Astrophys.* **654**, A27 (2021).
30. Gómez, J. L. et al. Probing the innermost regions of AGN Jets and their magnetic fields with RadioAstron. V. Space and ground millimeter-VLBI imaging of OJ 287. *Astrophys. J.* **924**, 122 (2022).
31. Bruni, G. et al. The RadioAstron dedicated DiFX dstribution. *Galaxies* **4**, 55 (2016).
32. Greisen, E. W. in *Information Handling in Astronomy—Historical Vistas* Astrophysics and Space Science Library Vol. 285 (ed. Heck, A.) 109–125 (Springer, 2003).
33. Kettenis, M., van Langevelde, H. J., Reynolds, C. & Cotton, B. ParselTongue: AIPS talking Python. In *Astronomical Data Analysis Software and Systems XV* Conference Series Vol. 351 (eds Gabriel, C. et al.) 497–500 (Astronomical Society of the Pacific, 2006).
34. Akiyama, K. et al. Superresolution full-polarimetric imaging for radio interferometry with sparse modeling. *Astron. J.* **153**, 159 (2017).
35. Akiyama, K. et al. Imaging the Schwarzschild-radius-scale structure of M87 with the Event Horizon Telescope using sparse modeling. *Astrophys. J.* **838**, 1 (2017).
36. Cho, I. et al. A comparative study of amplitude calibrations for the East Asia VLBI Network: a priori and template spectrum methods. *Publ. Astron. Soc. Jpn* **69**, 87 (2017).
37. Narayan, R. & Nityananda, R. Maximum entropy image restoration in astronomy. *Ann. Rev. Astron. Astrophys.* **24**, 127–170 (1986).
38. Högbom, J. A. Aperture synthesis with a non-regular distribution of interferometer baselines. *Astron. Astrophys. Suppl. Ser.* **15**, 417–426 (1974).

39. Shepherd, M. C. Difmap: an interactive program for synthesis imaging. In *Astronomical Data Analysis Software and Systems VI* Conference Series Vol. 125 (eds Hunt, G. & Payne, H.) 77–84 (Astronomical Society of the Pacific, 1997).
40. Event Horizon Telescope Collaboration et al. First Sagittarius A* Event Horizon Telescope results. III. Imaging of the galactic center supermassive black hole. *Astrophys. J. Lett.* **930**, L14 (2022).
41. Event Horizon Telescope Collaboration et al. First M87 Event Horizon Telescope results. VII. Polarization of the ring. *Astrophys. J. Lett.* **910**, L12 (2021).
42. Holdaway, M. A. & Wardle, J. F. C. Maximum entropy imaging of polarization in very long baseline interferometry. In *Digital Image Synthesis and Inverse Optics* Conference Series Vol. 1351 (eds Gmitro, A. F. et al.) 714–724 (SPIE, 1990).
43. Hovatta, T. et al. MOJAVE: monitoring of jets in active galactic nuclei with VLBA experiments. VIII. Faraday rotation in parsec-scale AGN jets. *Astron. J.* **144**, 105 (2012).
44. Park, J. et al. Revealing the nature of blazar radio cores through multifrequency polarization observations with the Korean VLBI Network. *Astrophys. J.* **860**, 112 (2018).
45. Newville, M. et al. lmfit/lmfit-py: 1.0.3. *Zenodo* https://doi.org/10.5281/zenodo.5570790 (2021).
46. Marziani, P., Sulentic, J. W., Dultzin-Hacyan, D., Calvani, M. & Moles, M. Comparative analysis of the high- and low-ionization lines in the broad-line region of active galactic nuclei. *Astrophys. J. Suppl. Ser.* **104**, 37–70 (1996).
47. Planck Collaboration et al. Planck 2015 results. XIII. Cosmological parameters. *Astron. Astrophys.* **594**, A13 (2016).
48. Nilsson, K., Pursimo, T., Villforth, C., Lindfors, E. & Takalo, L. O. The host galaxy of 3C 279. *Astron. Astrophys.* **505**, 601–604 (2009).
49. Bardeen, J. M. & Petterson, J. A. The lense-thirring effect and accretion disks around Kerr black holes. *Astrophys. J. Lett.* **195**, L65–L67 (1975).
50. Morgan, C. W., Kochanek, C. S., Morgan, N. D. & Falco, E. E. The quasar accretion disk size-black hole mass relation. *Astrophys. J.* **712**, 1129–1136 (2010).
51. Mizuno, Y., Lyubarsky, Y., Nishikawa, K.-I. & Hardee, P. E. Three-dimensional relativistic magnetohydrodynamic simulations of current-driven instability. III. Rotating relativistic jets. *Astrophys. J.* **757**, 16 (2012).
52. Perucho, M. Dissipative processes and their role in the evolution of radio galaxies. *Galaxies* **7**, 70 (2019).
53. Hardee, P. E. Spatial stability of jets: the nonaxisymmetric fundamental and reflection modes. *Astrophys. J.* **313**, 607 (1987).
54. Rybicki, G. B. & Lightman, A. P. *Radiative Processes in Astrophysics* (Wiley, 1979).
55. Lyutikov, M., Pariev, V. I. & Gabuzda, D. C. Polarization and structure of relativistic parsec-scale AGN jets. *Mon. Not. R. Astron. Soc.* **360**, 869–891 (2005).

Acknowledgements

We thank L. Hermosa for useful comments on the manuscript. The work at the IAA-CSIC was supported in part by the Spanish Ministerio de Economía y Competitividad (grant numbers AYA2016-80889-P and PID2019-108995GB-C21), the Consejería de Economía, Conocimiento, Empresas y Universidad of the Junta de Andalucía (grant number P18-FR-1769), the Consejo Superior de Investigaciones Científicas (grant number 2019AEP112), the State Agency for Research of the Spanish MCIU through the 'Center of Excellence Severo Ochoa' award to the Instituto de Astrofísica de Andalucía (grant number SEV-2017-0709) and grant number CEX2021-001131-S funded by MCIN/AEI/10.13039/501100011033. J.M.M. and M.P. acknowledge support from the Spanish Ministerio de Ciencia through grant number PID2019-107427GB-C33 and from the Generalitat Valenciana through grant number PROMETEU/2019/071. J.M.M. acknowledges additional support from the Spanish Ministerio de Economía y Competitividad through grant number PGC2018-095984-B-l00. M.P. acknowledges additional support from the Spanish Ministerio de Ciencia through grant number PID2019-105510GB-C31. Y.Y.K. was supported by Russian Science Foundation grant number 21-12-00241. A.C. is an Einstein Fellow of the NASA Hubble Fellowship Program (grant number HST-HF2-51431.001-A), awarded by the Space Telescope Science Institute, which is operated by the Association of Universities for Research in Astronomy, Inc., for NASA, under contract number NAS5-26555. J.-Y.K. was supported in this research by the National Research Foundation of Korea (NRF) under a grant funded by the Korean government (Ministry of Science and ICT; grant number 2022R1C1C1005255). Y.M. acknowledges support from the National Natural Science Foundation of China (grant number 12273022) and the Shanghai pilot programme of international scientist for basic research (grant number 22JC1410600). T.S. was supported by the Academy of Finland projects 274477, 284495, 312496 and 315721. The RadioAstron project is led by the Astro Space Center of the Lebedev Physical Institute of the Russian Academy of Sciences and the Lavochkin Scientific and Production Association under a contract with the Russian Federal Space Agency, in collaboration with partner organizations in Russia and other countries. The European VLBI Network is a joint facility of independent European, African, Asian, and North American radio astronomy institutes. Scientific results from data presented in this publication are derived from the EVN project code GA030D. This research is partly based on observations with the 100 m telescope of the MPIfR at Effelsberg. This publication makes use of data obtained at Metsähovi Radio Observatory, operated by Aalto University in Finland. Our special thanks go to the people supporting the observations at the telescopes during the data collection. This research is based on observations correlated at the Bonn Correlator, jointly operated by the Max-Planck-Institut für Radioastronomie, and the Federal Agency for Cartography and Geodesy. This study makes use of 43 GHz VLBA data from the VLBA-BU Blazar Monitoring Program (VLBA-BU-BLAZAR; http://www.bu.edu/blazars/BEAM-ME.html), funded by NASA through Fermi Guest Investigator grant number 80NSSC20K1567.

Author contributions

A.F., J.L.G. and G.Y.-Z. worked on the data calibration. A.F., J.L.G., G.Y.-Z., R.L., A.C., K.A., K.L.B, H.S., I.C. and E.T. worked on the image reconstruction and analysis. G.B. correlated the space VLBI data. J.M.M., M.P., A.F., J.L.G. and Y.M worked on the interpretation of the results. All authors contributed to the discussion of the results presented and commented on the manuscript.

Competing interests

The authors declare no competing interests.

Additional information

Extended data is available for this paper at https://doi.org/10.1038/s41550-023-02105-7.

Correspondence and requests for materials should be addressed to Antonio Fuentes or José L. Gómez.

Peer review information *Nature Astronomy* thanks the anonymous reviewers for their contribution to the peer review of this work.

[1]Instituto de Astrofísica de Andalucía (CSIC), Granada, Spain. [2]Departament d'Astronomia i Astrofísica, Universitat de València, Burjassot, Spain. [3]Observatori Astronòmic, Universitat de València, Paterna, Spain. [4]Istituto di Radioastronomia, INAF, Bologna, Italy. [5]Max-Planck-Institut für Radioastronomie, Bonn, Germany. [6]Istituto di Astrofisica e Planetologia Spaziali, INAF, Rome, Italy. [7]Lebedev Physical Institute of the Russian Academy of Sciences, Moscow, Russia. [8]Princeton Gravity Initiative, Princeton University, Princeton, NJ, USA. [9]Haystack Observatory, Massachusetts Institute of Technology, Westford, MA, USA. [10]National Astronomical Observatory of Japan, Mitaka, Japan. [11]Black Hole Initiative at Harvard University, Cambridge, MA, USA. [12]California Institute of Technology, Pasadena, CA, USA. [13]Indian Institute of Science Education and Research Kolkata, Mohanpur, India. [14]Joint Institute for VLBI ERIC (JIVE), Dwingeloo, The Netherlands. [15]Aerospace Faculty, Delft University of Technology, Delft, The Netherlands. [16]Institute for Astrophysical Research, Boston University, Boston, MA, USA. [17]Astronomical Institute, St. Petersburg State University, St. Petersburg, Russia. [18]Department of Astronomy and Atmospheric Sciences, Kyungpook National University, Daegu, Republic of Korea. [19]Korea Astronomy and Space Science Institute, Daejeon, Republic of Korea. [20]Tsung-Dao Lee Institute, Shanghai Jiao Tong University, Shanghai, People's Republic of China. [21]School of Physics and Astronomy, Shanghai Jiao Tong University, Shanghai, People's Republic of China. [22]Institut für Theoretische Physik, Goethe-Universit ät Frankfurt, Frankfurt am Main, Germany. [23]Department of Electronics and Nanoengineering, Aalto University, Aalto, Finland. [24]Metsähovi Radio Observatory, Aalto University, Kylmälä, Finland. ✉e-mail: afuentes@iaa.es; jlgomez@iaa.es

https://doi.org/10.1038/s41550-023-02105-7

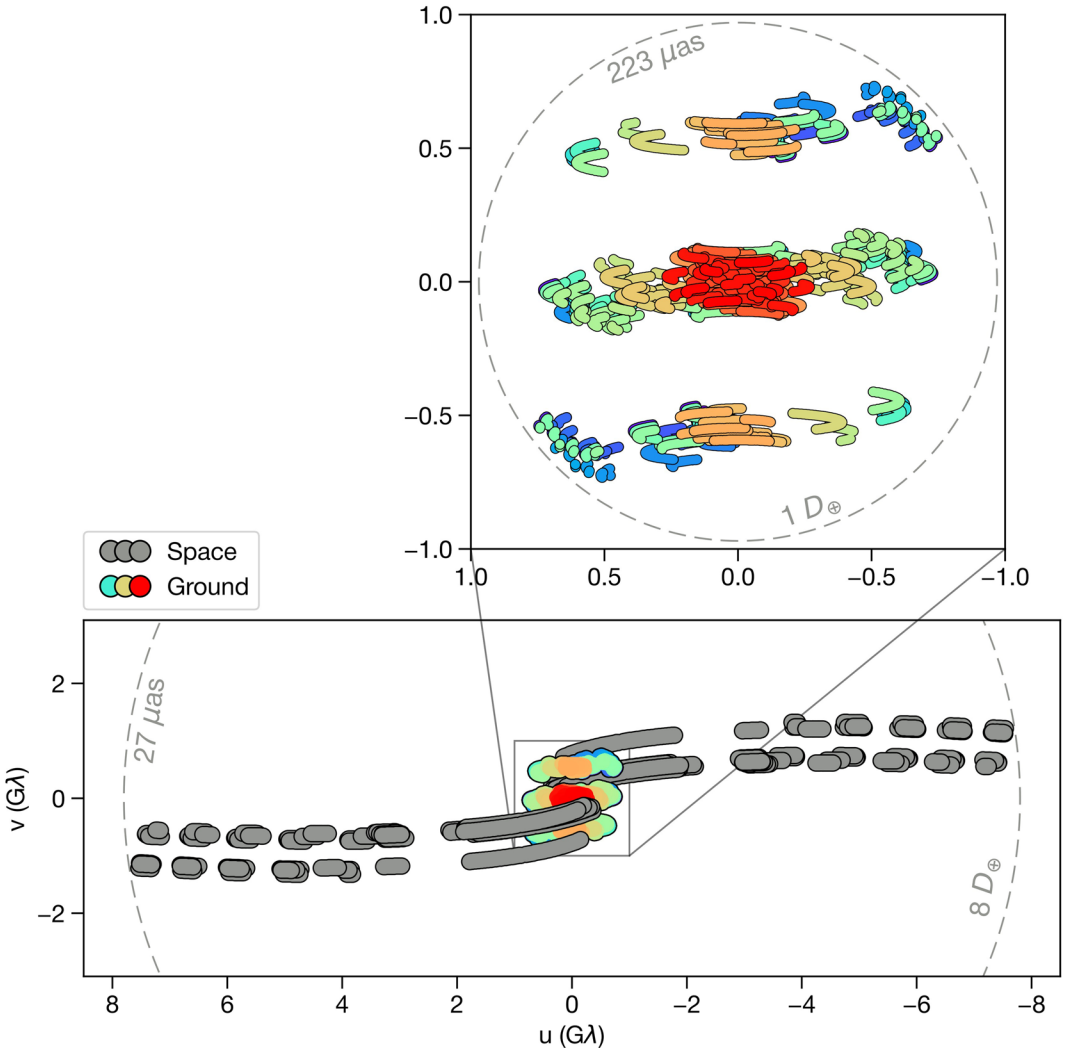

Extended Data Fig. 1 | Baseline coverage for our *RadioAstron* observations of 3C 279 in March 2014. Rainbow-coloured and grey points indicate individual ground-ground baselines and space-ground baselines, respectively. Dashed circles indicate the baseline length in Earth's diameter units ($D_\oplus$) and the corresponding angular resolution.

https://doi.org/10.1038/s41550-023-02105-7

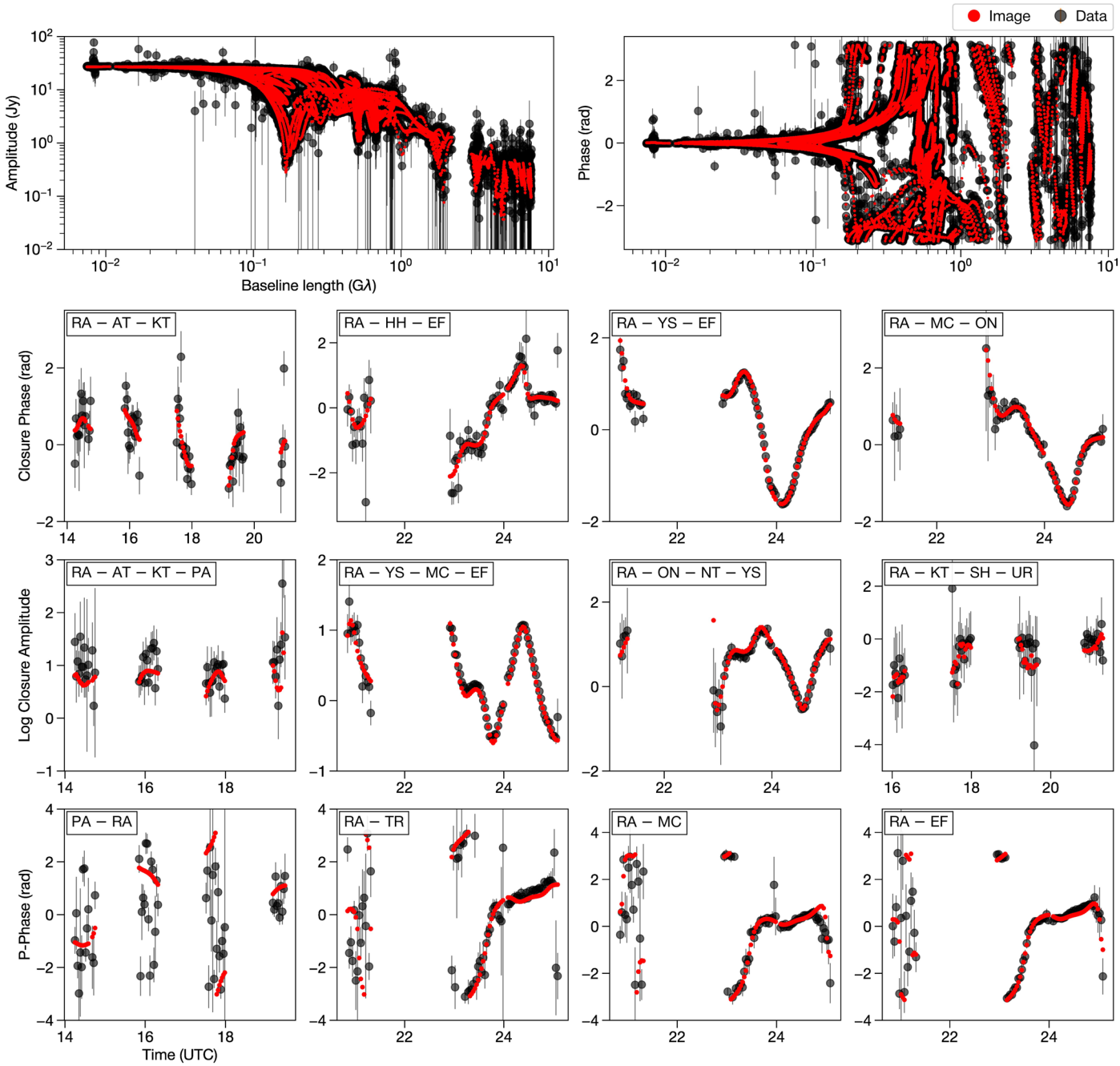

Extended Data Fig. 2 | Fitting of the polarimetric *RadioAstron* image to a selection of data products. Two minute time-averaged data (black points) and image model (red points) self-calibrated visibility amplitudes and phases, closure phases, log closure amplitudes, and polarimetric visibility phases as a function of time. Error bars indicate ± 1σ uncertainty from thermal noise plus 1.5 % non-closing error uncertainties added in quadrature. All these examples include *RadioAstron* measurements.

https://doi.org/10.1038/s41550-023-02105-7

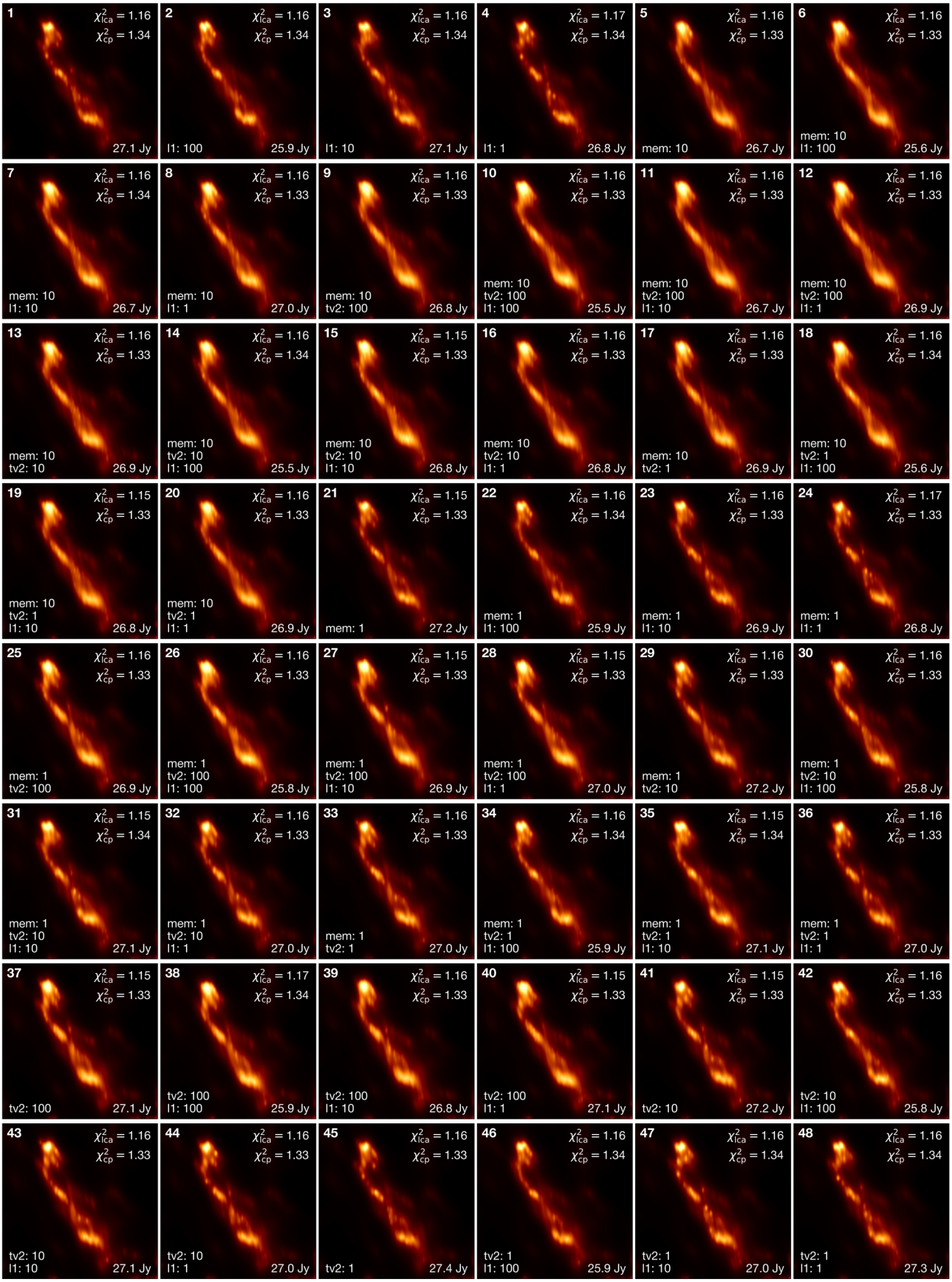

Extended Data Fig. 3 | Top 48 image reconstructions from the parameter survey conducted. Each image includes the closure phase (cp) and log closure amplitude (lca) reduced χ^2, the image regularizers used and their weight, and the total flux reconstructed.

https://doi.org/10.1038/s41550-023-02105-7

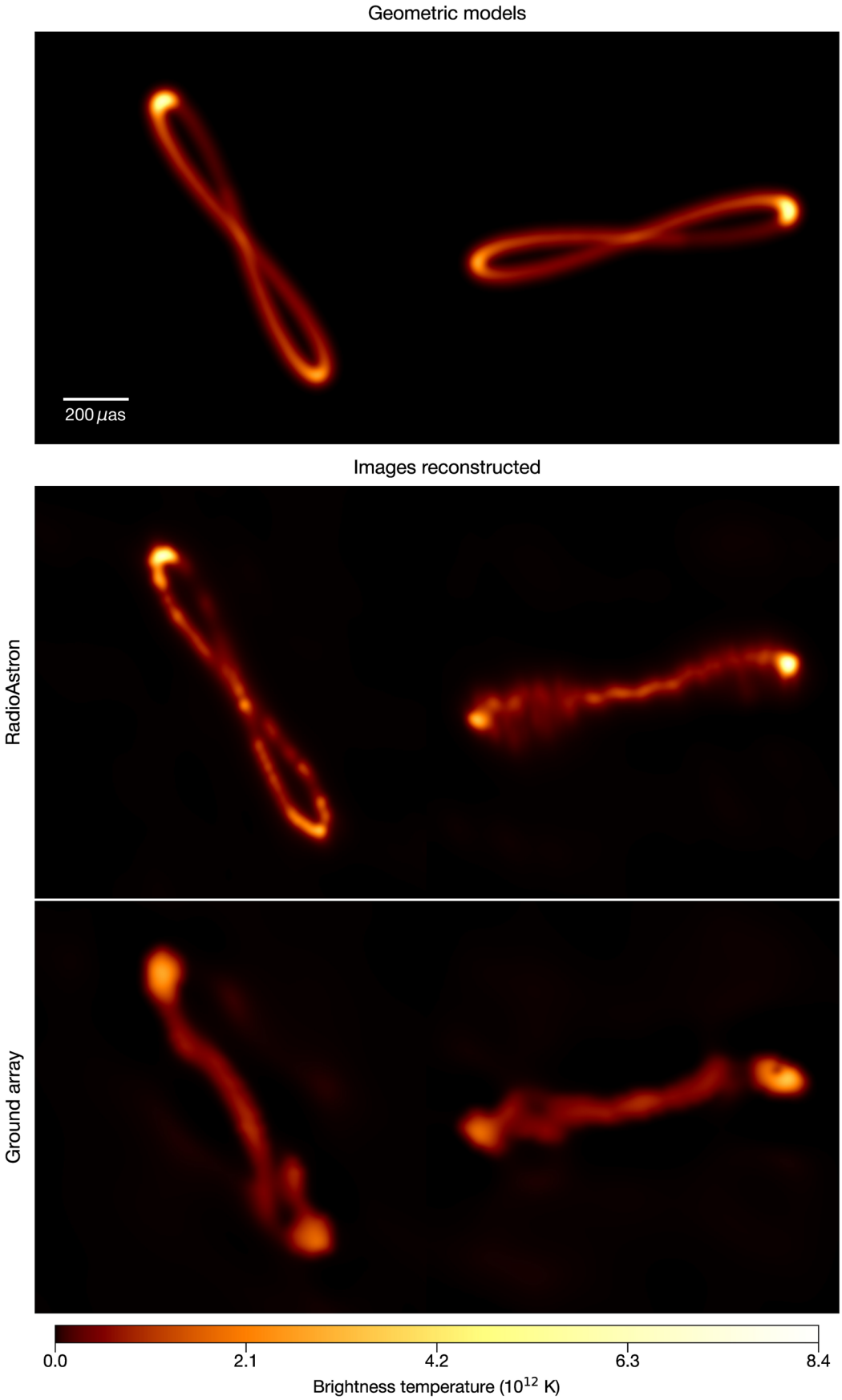

Extended Data Fig. 4 | Synthetic data tests. In the top row we present the geometric models used to generate the synthetic data. In the middle and bottom rows we show, respectively, the images reconstructed from each data set when *RadioAstron* is included in the array and when only ground stations participate.